INTERNATIONAL JOURNAL FOR NUMERICAL METHODS IN FLUIDS, VOL. 15, 427–451 (1992)

# EULER SOLUTIONS FOR SELF-GENERATED ROTOR BLADE–VORTEX INTERACTIONS*

A. A. HASSAN

*Aerodynamics/Acoustics, McDonnell Douglas Helicopter Company, 5000 East McDowell Road, Mesa, AZ 85205–9797, U.S.A.*

C. TUNG

*Aeroflightdynamics Directorate, AVSCOM, NASA Ames Research Center, Moffett Field, CA, U.S.A.*

AND

L. N. SANKAR

*School of Aerospace Engineering, Georgia Institute of Technology, Atlanta, GA, U.S.A.*

## SUMMARY

A finite-difference procedure has been developed for the prediction of three-dimensional rotor blade–vortex interactions. The interaction velocity field was obtained through a non-linear superposition of the rotor flow field, computed using the unsteady three-dimensional Euler equations, and the embedded vortex wake flow field, computed using the law of Biot–Savart. In the Euler model, near wake rotational effects were simulated using the surface velocity 'transpiration' approach. As a result, a modified surface boundary condition was prescribed and enforced at each time step of the computations to satisfy the tangency boundary condition. For supercritical interactions using an upstream-generated vortex, accuracy of the numerical results were found to rely on the user-specified vortex core radius and vortex strength. For the more general self-generated subcritical interactions, vortex wake trajectories were computed using the lifting-line helicopter/rotor trim code CAMRAD. For these interactions, accuracy of the results were found to rely heavily on the CAMRAD-predicted vortex strength, vortex orientation with respect to the blade, and to a large extent on the user-specified vortex core radius. Results for the one-seventh scale model OLS rotor and for a non-lifting rectangular blade having a NACA0012 section are presented. Comparisons with the experimental wind-tunnel data are also made.

KEY WORDS Aerodynamics Rotor Blade–vortex Interactions

## INTRODUCTION

The flow field of a modern rotary wing aircraft is highly unsteady and three-dimensional. Under certain flight conditions, and, in particular, low-speed descent, close encounters between the blade and the trailing tip vortex of a preceding blade, or even the same blade, take place. These close encounters commonly referred to as blade–vortex interactions, or BVI, result in significant impulsive changes in the rotor blade aerodynamic loads which lead to an increase in vibration and noise levels. To date, a large number of experimental set-ups[1–4] have successfully mimicked

* Presented as AIAA paper 90–1588 at the AIAA 20th Fluids and Plasma Dynamics Conference, Buffalo, New York, June 1990.

0271–2091/92/160427–25$17.50

*Received 16 August 1990*
*Revised 27 January 1992*

idealized conditions for these interactions. For example, in Reference 2 parallel and oblique-type BVI were simulated using an upstream-generated vortex which interacts with a non-lifting rotor (i.e. in the absence of a rotor-generated wake) at a predetermined rotor azimuth, vortex orientation, and vortex miss distance. In these experiments, the experimental parameters relating to the vortex (e.g. the vortex strength, core radius, and orientation with respect to the blade) are all defined through local flow measurements and visualization techniques. For the self-generated interactions considered in this paper, these parameters are not known *a priori* and, therefore, they must be determined numerically.

In recent years, numerical simulations of three-dimensional BVI have been limited to duplicating the idealized wind-tunnel single-vortex interaction (parallel or oblique) experiments using a non-lifting rotor. However, in contrast to the conditions duplicated in these experiments, the lifting rotor environment is one which involves multiple-vortex interactions some of which are near parallel (i.e. the vortex axis is almost parallel to the blade's leading edge), some are oblique, and some are almost perpendicular (i.e. the vortex axis is perpendicular to the blade's leading edge at a given azimuth and radial station). Moreover, self-generated wake elements are usually curved and non-planar. As a result, it is quite difficult to identify in this context 'a single-vortex miss distance' since for each point on the vortex element the associated miss distance is a function of the rotor azimuth position (or equivalently time), and the chordwise and spanwise positions along the blade.

In the numerical simulations of BVI two fundamental issues usually arise. The first, relates to the selection of an appropriate mathematical model which accurately describes the velocity distribution in the core of the vortex and, hence, the vortex-induced velocity field. The second, deals with the numerical approach to be adopted for modelling the trailing tip vortex flow field within a particular mathematical formulation. The first issue is usually resolved through the introduction of analytic vortex core models into the numerical simulations (e.g. the one by Scully[5] and the Lamb-like vortex core model used by Srinivasan[6]). In addressing the second issue, four different approaches varying in their degree of complexity and computational requirements have been adopted by researchers in various formulations (e.g. full potential, Euler and Navier–Stokes) to model the flow field of embedded vortex wakes in the aerofoil–vortex or blade–vortex interaction problems. These four approaches are commonly referred to in the literature as (1) the 'angle of attack' approach, (2) the lifting surface or velocity 'transpiration' approach, (3) the 'branch cut' approach and (4) the split potential or 'perturbation' approach.

The first and second approaches are by far the simplest to implement in any existing two- or three-dimensional mathematical formulation. In the first approach, vortex effects are represented by a single change in the aerofoil's (or blade section) angle of attack. In the second approach, vortex effects are represented by a continuous chordwise variation of the vortex-induced normal velocities at the surface of the aerofoil or blade. In this respect, the effect of the external disturbances introduced by the vortex are only felt through the surface boundary condition. In inviscid computations, the surface boundary condition in turn must be modified to satisfy the 'slip' flow condition at the surface of the blade. In this work, we utilize the first approach to model the global effects of the far-wake-induced inflow at the quarter-chord points of the various sections constituting the rotor blade. The angles of attack are computed using Scully's free wake model in the lifting-line helicopter/rotor trim code CAMRAD.[7] Among the solution procedures adopting the second approach we mention those of Sankar and Malone,[8] Jones,[9] Sankar and Tung,[10] and Hassan and Charles.[11,12]

In the third approach, most suitable for potential formulations, artificial surfaces of discontinuity (and, hence, the notation 'branch cut' approach) are introduced into the flow solution domain. The jump in the potential function across these surfaces is set equal to the strength of the

'embedded' vortex. This approach, though mathematically elegant and quite accurate, requires a large amount of numerical book keeping and becomes tedious when the surfaces of discontinuity do not coincide or align with the grid lines or grid surfaces in the computational domain.[13,14] For example, for curved wakes such as those generated at the blade tip, an adaptive grid which deforms to conform to the curvature of the wake is necessary in order to avoid the cumbersome effort required to interpolate for the instantaneous wake position and induced velocities at the otherwise rigid grid points. As a result, the implementation of this approach to model BVI has been limited to two-dimensional flows.[9,15,16]

The fourth approach (perturbation) was first suggested by Steinhoff and Suryanarayanan[17] and has been successfully applied in the numerical simulations of two- and three-dimensional BVI problems. In this approach, the velocity potential function, or any of the dependent flow variables for higher-order mathematical models, are decomposed into two parts; the first represents the perturbation due solely to the flow past the aerofoil or blade, and the second represents the potential (or the magnitude of the dependent flow variables) describing the vortex flow field. A simple algebraic manipulation of the definition of the potential function, or the dependent variables, in the governing equation(s) results in a similar set of equation(s) for the perturbation quantities which are then solved for. Among the solution procedures utilizing this approach are those of Jones,[9] Baeder *et al.*,[18] Caradonna *et al.*,[19] Damodaran and Caughey,[20] and Srinivasan *et al.*[21]

In light of the above discussion, and in the interest of keeping the analysis simple and inexpensive, it was concluded that the velocity transpiration approach is more suitable for modelling the complex self-generated three-dimensional BVI problem. As mentioned earlier, this approach, requires the computation of the vortex-induced velocities only at grid point locations lying on the surface of the blade, and the modification of the slip surface boundary condition in the unsteady Euler formulation. In contrast, the split potential approach was not implemented on the account of its large computer CPU and memory requirements which are dictated by the necessity to compute the vortex-induced velocities (or equivalently a potential function) at every grid node inside the computational domain. It is also noteworthy to mention that Jones,[9] using the two-dimensional full potential equation, has shown that almost identical results are obtained when using the transpiration, split potential, and vortex embedding approaches in the modelling of the aerofoil-vortex interaction problem.

Very recently, using the velocity transpiration approach, Hassan and Charles[11,12] demonstrated the effectiveness and relative accuracy of using a full potential formulation in the modelling of rotor self-generated BVI. In this paper, we adapt their BVI modelling technique for the more comprehensive Euler equations. In this paper, two distinct BVI problems will be addressed. The supercritical parallel BVI model problem of Reference 1 for a non-lifting rectangular blade having a NACA0012 section, and the subcritical self-generated BVI problem for a lifting one-seventh scale AH1-OLS model rotor.[22,23]

## GOVERNING EQUATIONS

The numerical simulations were performed using an Euler rotor flow solver designated 'EULR.BVI'. This solver is a modified version of the unsteady three-dimensional, Euler/Navier–Stokes (N–S) rotor code 'NAV3D' developed by Wake and Sankar.[24] The governing partial differential equations are the unsteady three-dimensional Euler equations for a perfect gas. These are expressed in non-dimensional strong conservation-law form as

$$\mathbf{q}_t + \mathbf{E}_x + \mathbf{F}_y + \mathbf{G}_z = \mathbf{0}, \tag{1}$$

where

$$\begin{aligned}
\mathbf{q} &= [\rho\ \rho u\ \rho v\ \rho we]^{\mathrm{T}},\\
\mathbf{E} &= [\rho u(\rho u^2+p)\ \rho uv\ \rho uw\ u(p+e)]^{\mathrm{T}},\\
\mathbf{F} &= [\rho v\ \rho uv(\rho v^2+p)\ \rho vw\ v(p+e)]^{\mathrm{T}},\\
\mathbf{G} &= [\rho w\ \rho uw\ \rho vw(\rho w^2+p)\ w(p+e)]^{\mathrm{T}}.
\end{aligned} \tag{2}$$

In equation (2), the local density $\rho$ has been normalized by the free-stream density, local inertial velocity components by the free-stream speed of sound, pressure $p$ and total energy per unit volume $e$ by the dynamic pressure (based on free stream speed of sound and free stream density), and distances $x, y, z$ by the blade chord length $C$. For a calorically perfect gas, the equation of state may be written as

$$p=(\gamma-1)\,[e-0{\cdot}5\,(u^2+v^2+w^2)]. \tag{3}$$

To facilitate the application of surface boundary conditions and the treatment of arbitrary blade geometries, we consider a co-ordinate transformation of the form

$$\begin{aligned}
\xi &= \xi(x, y, z, t),\\
\eta &= \eta(x, y, z, t),\\
\zeta &= \zeta(x, y, z, t),\\
\tau &= t,
\end{aligned} \tag{4}$$

where the $\xi$-direction is aligned with the blade chordwise direction $x$, the $\eta$-direction with the spanwise or radial direction $y$, and the $\zeta$-direction roughly with the normal direction to the blade $z$. With $\xi$, $\eta$, $\zeta$ and $\tau$ as new independent variables, we rewrite equations (1) and (2) as

$$\mathbf{q}_\tau+\mathbf{E}_\xi+\mathbf{F}_\eta+\mathbf{G}_\zeta=\mathbf{0}, \tag{5}$$

$$\begin{aligned}
\mathbf{q} &= \mathbf{q}J^{-1},\\
\mathbf{E} &= (\xi_t\mathbf{q}+\xi_x\mathbf{E}+\xi_y\mathbf{F}+\xi_z\mathbf{G})J^{-1},\\
\mathbf{F} &= (\eta_t\mathbf{q}+\eta_x\mathbf{E}+\eta_y\mathbf{F}+\eta_z\mathbf{G})J^{-1},\\
\mathbf{G} &= (\zeta_t\mathbf{q}+\zeta_x\mathbf{E}+\zeta_y\mathbf{F}+\zeta_z\mathbf{G})J^{-1},
\end{aligned} \tag{6}$$

In equation (6), $\xi_x$, $\xi_y$, $\xi_z$, $\eta_x$, . . . , etc are the metrics of the co-ordinate transformation which are related to the physical plane co-ordinates $x$, $y$, $z$ via

$$\begin{bmatrix} \xi_x & \xi_y & \xi_z \\ \eta_x & \eta_y & \eta_z \\ \zeta_x & \zeta_y & \zeta_z \end{bmatrix} = \begin{bmatrix} x_\xi & x_\eta & x_\zeta \\ y_\xi & y_\eta & y_\zeta \\ z_\xi & z_\eta & z_\zeta \end{bmatrix}^{-1}.$$

$J$ is the Jacobian of the co-ordinate transformation:

$$J=\xi_x(\eta_y\zeta_z-\eta_z\zeta_y)+\xi_y(\eta_z\zeta_x-\eta_x\zeta_z)+\xi_z(\eta_x\zeta_y-\eta_y\zeta_x),$$

and $U$, $V$, and $W$ are the contravariant velocity components, viz.

$$\begin{aligned}
U &= \xi_t+\xi_x u+\xi_y v+\xi_z w,\\
V &= \eta_t+\eta_x u+\eta_y v+\eta_z w,\\
W &= \zeta_t+\zeta_x u+\zeta_y v+\zeta_z w.
\end{aligned}$$

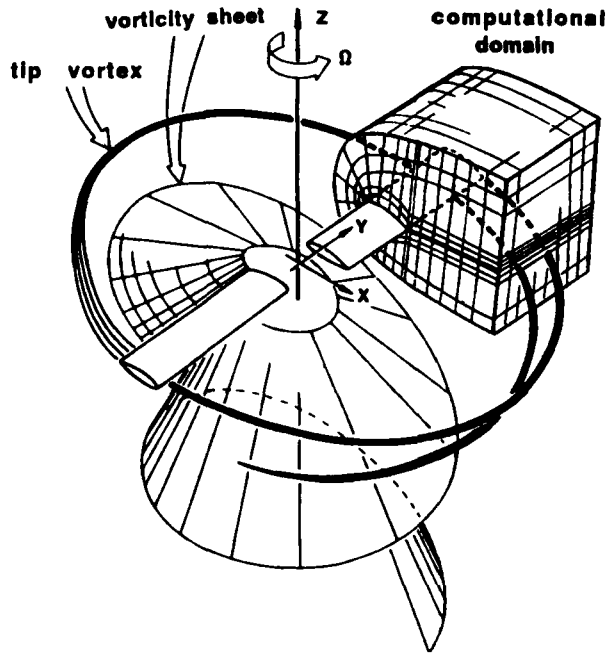


Figure 1. Schematic representation of a two-bladed rotor, its wake system, and computational domain

Equation (5) is first discretized and then solved on a three-dimensional computational grid. The three-dimensional rigid grid (attached to the blade in the rotating blade-fixed co-ordinate system) was constructed by the interpolation and subsequent stacking of two-dimensional near orthogonal sheared parabolic C-type grids generated at user-selected blade radial stations, see Figure 1. The two-dimensional grids were constructed using Jameson's[25] algebraic grid generation procedure built into the Euler rotor flow solver.

## NUMERICAL ALGORITHM

A hybrid (implicit–explicit) ADI scheme is used to solve the discretized forms of equation (5). The flux terms in the $\xi$ (chordwise) and the $\zeta$ (transverse direction) are treated implicitly. In the $\eta$ (spanwise) direction, the flux terms are treated explicitly using the most recent values of the computed-dependent variables. This solution algorithm results in two-block matrix operators instead of the usual three which typically exist in fully implicit schemes. Consequently, the CPU time requirements for the hybrid scheme are approximately 30% less than those required for a fully comparable implicit scheme.

Equation (5) is discretized in time using two-point backward first-order differencing, and in space using standard three-point second-order central differencing, i.e.

$$\mathbf{q}^{n+1} = \mathbf{q}^n - \Delta\tau(\delta_\xi \mathbf{E}^{n+1} + \delta_\eta \mathbf{F}^{n,n+1} + \delta_\zeta \mathbf{G}^{n+1}). \tag{7}$$

In Equation (7) $\delta$ is a three-point central differencing operator, and $n$ and $(n+1)$ represent two consecutive time levels (e.g. old and new, respectively). Equation (7) is highly non-linear since the flux terms $\mathbf{E}$ and $\mathbf{G}$ are functions of the dependent variable $\mathbf{q}$. Application of Taylor series

expansion to these terms result in the following linearized expressions for **E** and **G** at the new time level $(n+1)$, viz.

$$\mathbf{E}^{n+1} = \mathbf{E}^n + [\mathbf{A}]^n \Delta\mathbf{q}^{n+1},$$
$$\mathbf{G}^{n+1} = \mathbf{G}^n + [\mathbf{C}]^n \Delta\mathbf{q}^{n+1}, \tag{8}$$

where

$$\Delta\mathbf{q}^{n+1} = \mathbf{q}^{n+1} - \mathbf{q}^n,$$
$$[\mathbf{A}]^n = (\partial_q \mathbf{E})^n, \tag{9}$$
$$[\mathbf{C}]^n = (\partial_q \mathbf{G})^n.$$

In equation (8), [**A**] and [**C**] are commonly referred to as the 'Jacobian matrices' of the flux vectors **E** and **G**. The coefficients in these two matrices are computed using analytic expressions which are obtained through partial differentiation of the vectors given in equation (6) with respect to the appropriate dependent variable. Rewriting equation (7) after utilizing the expressions given in equations (8) and (9) and rearranging, we obtain the following system of linear equations for $\Delta\mathbf{q}$:

$$[\mathbf{I} + \Delta\tau(\delta_\xi \mathbf{A}^n + \delta_\zeta \mathbf{C}^n)]\Delta\mathbf{q}^{n+1} = [\mathbf{RHS}]^{n,n+1}. \tag{10}$$

In equation (10), **I** is the identity matrix and [**RHS**] is given by

$$[\mathbf{RHS}]^{n,n+1} = -\Delta\tau(\delta_\xi \mathbf{E}^n + \delta_\eta \mathbf{F}^{n,n+1} + \delta_\zeta \mathbf{G}^n). \tag{11}$$

The Beam and Warming[26] approximate factorization scheme is then used to approximate the two-dimensional spatial differential operator appearing on the left-hand side of equation (10) as the product of two one-dimensional spatial operators in the $\xi$, $\zeta$ directions, i.e.

$$[\mathbf{I} + \Delta\tau\delta_\xi \mathbf{A}^n][\mathbf{I} + \Delta\tau\delta_\zeta \mathbf{C}^n]\Delta\mathbf{q}^{n+1} = [\mathbf{RHS}]^{n+1}. \tag{12}$$

Solutions to equation (12) are then obtained using a two-step process each involving the inversion of a block tridiagonal matrix (having $5 \times 5$ coefficient matrices). Let $\Delta\mathbf{s}$ be an intermediate solution vector defined by

$$\Delta\mathbf{s}^{n+1} = [\mathbf{I} + \Delta\tau\,\delta_\zeta \mathbf{C}^n]\Delta\mathbf{q}^{n+1}, \tag{13}$$

then equation (12) can be reduced to

$$[\mathbf{I} + \Delta\tau\,\delta_\xi \mathbf{A}^n]\Delta\mathbf{S}^{n+1} = [\mathbf{RHS}]^{n,n+1}. \tag{14}$$

Successive application of equation (14) followed by the application of equation (13) result in the new value for the vector $\Delta\mathbf{q}$ at the $(n+1)$ time level. This process is repeated at each computational spanwise station along the blade. However, to eliminate any dependency of the numerical solutions on the spanwise 'marching' direction, the solutions are allowed to advance from the most inboard computational station towards the outermost spanwise station at one time level and vice versa at the next time level (i.e. from the outermost station towards the innermost station). More precisely, when sweeping towards the blade tip, we evaluate the second term on the right-hand side of equation (11) as

$$\delta_\eta \mathbf{F}^{n,n+1} = 0{\cdot}5\,[\mathbf{F}^n(i, j+1, k) - \mathbf{F}^{n+1}(i, j-1, k)].$$

When sweeping towards the root of the blade, this term is evaluated as

$$\delta_\eta \mathbf{F}^{n,n+1} = 0{\cdot}5\,[\mathbf{F}^{n+1}(i, j+1, k) - \mathbf{F}^n(i, j-1, k)].$$

To prevent the odd–even point decoupling which results from the use of central difference operators on the left-hand side of equation (12), and to suppress the appearance of spurious solution oscillations in the vicinity of shock waves and stagnation points, second- and fourth-order dissipation terms[27] in the $\xi$, $\zeta$ directions are added to these equations. More precisely, implicit second-order and explicit fourth-order dissipation terms are added, respectively, to the left- and right-hand sides of equations (13) and (14), i.e.

$$[\mathbf{I}+\Delta\tau\delta_\xi\mathbf{A}^n-\Delta\tau\varepsilon_i J^{-1}\nabla_\xi\Delta_\xi J]\,\Delta\mathbf{s}^{n+1}=[\mathrm{RHS}]^{n,n+1}-D_e^{n,n+1}, \tag{15}$$

$$[\mathbf{I}+\Delta\tau\delta_\zeta\mathbf{C}^n-\Delta\tau\varepsilon_i J^{-1}\nabla_\zeta\Delta_\zeta J]\,\Delta\mathbf{q}^{n+1}=\Delta\mathbf{s}^{n+1}. \tag{16}$$

In equations (15) and (16), $\nabla_\xi$, and $\Delta_\xi$ are one-sided first-order finite-difference operators. The explicit dissipation term $D_e$ is given by

$$D_e^{n,n+1}=\Delta\tau\varepsilon_e J^{-1}[(\nabla_\xi\Delta_\xi)^2+(\nabla_\eta\Delta_\eta)^2+(\nabla_\zeta\Delta_\zeta)^2]J\mathbf{q}^n.$$

The magnitude of the implicit dissipation coefficient $\varepsilon_i$ is usually 3–5 times that of the explicit coefficient $\varepsilon_e$.

For quasi-steady solutions, equations (15) and (16) are advanced in time using a time step $\Delta\tau$ which is a function of the local transformation Jacobian,[28] i.e.

$$\Delta\tau=\frac{1}{1+J^{1/3}(i,j,k)}. \tag{17}$$

For unsteady calculations, the time step was set equal to the time required by the rotor to advance one-quarter of a degree of azimuth. Note that for the hybrid scheme adopted here, Von Neumann stability analysis indicate that the scheme is unconditionally stable.[29]

## NUMERICAL BOUNDARY CONDITIONS

The present formulation require boundary conditions to be specified along the blade's surface, trailing edge vortex sheet (commonly referred to as near wake or branch cut), far-field boundaries located outboard of the rotor tip, inflow boundary, outflow boundary beyond the blade's trailing edge, and the most inboard boundary of the computational region. For lifting conditions, the effects of the far wake (the portion of the wake which lies outside the bounds of the computational domain) must also be accounted for and modelled in the Euler solution. To simplify the numerical solution procedure, the boundary conditions are treated explicitly. That is, boundary values needed at the new time level $(n+1)$ are determined uniquely from the solution at the old time level $n$. More precisely, initially, the changes in the dependent variables $\Delta\mathbf{q}$ 'or delta quantities' are set equal to zero. However, at the end of each time step, the boundary conditions are updated using the solution values at the internal grid nodes. In the following, the numerical boundary conditions are briefly described.

*Far-field boundaries (inflow, outflow, outboard)*

For the Euler equations, advantage is taken of the characteristic features of a subsonic/supersonic inflow and/or outflow boundary.[30] The characteristics of the Euler equations *a priori* determine the number and type of variable(s) (e.g. $\rho$, $\rho u$, $\rho v$, $\rho w$, $e$) which can be specified at these boundaries. The remaining variables are then determined explicitly through extrapolation from the inner domain solutions and are found as part of the numerical solution.

For a subsonic inflow boundary, the variables $\rho u$, $\rho v$, $\rho w$, and $e$ are specified while the density is extrapolated from the interior. At the downstream (outflow) boundary, first-order extrapolation

of the conserved variables is used. At this boundary, the pressure is held fixed at its free stream value. For a supersonic inflow boundary, all variables are specified. For supersonic outflow, all information propagates out of the numerical integration domain. Therefore, all flow variables are extrapolated from within the computational domain.

*Inboard boundary*

Along this boundary, a condition stipulating zero gradient of the spanwise fluxes was enforced. This was accomplished here through assigning equal values to the dependent variables at the two inner most computational stations.

*Blade surface*

On the solid surface, the inviscid 'slip' boundary condition was enforced during the computations, viz.

$$\mathbf{V}\cdot\mathbf{n}=0 \tag{18}$$

where $\mathbf{n}$ is the outward unit vector normal to the surface of the blade and $\mathbf{V}$ is the local flow velocity vector. Since the present grid is nearly orthogonal everywhere, equation (18) is equivalent to setting $W=0$. This is due to the fact that the normal vector $\mathbf{n}$ is approximately aligned with the computational $\zeta$-direction. In the calculations, $u$ and $v$ were extrapolated from the interior. The density and pressure on the blade's surface were computed using simple one-sided differencing expressions, viz.

$$\rho(i, j, 1)=\tfrac{4}{3}\rho(i, j, 2)-\tfrac{1}{3}\rho(i, j, 3),$$

$$p(i, j, 1)=\tfrac{4}{3}p(i, j, 2)-\tfrac{1}{3}p(i, j, 3),$$

which represent a vanishing normal first derivative. The index $i$ represents all grid points lying on the surface of the blade between the trailing edge point on the lower surface and the trailing edge point on the upper surface. The index $j$ refers to all grid stations lying on the surface of the blade between the inner most computational station and the blade tip computational station.

In the present study for modelling blade–vortex interactions, equation (18) was modified to reflect the vortex-induced velocities at grid point locations lying on the surface of the blade, i.e.

$$(\mathbf{V}+\mathbf{V}_\mathrm{I})\cdot\mathbf{n}=0. \tag{19}$$

In equation (19), $\mathbf{V}_\mathrm{I}$ is the vortex-induced total velocity computed using the law of Biot–Savart,

$$\mathrm{d}\mathbf{V}_\mathrm{I}=\frac{\Gamma(\mathrm{d}\boldsymbol{l}\times\mathbf{r})}{4\pi r^3}. \tag{20}$$

Note that the net effect of the near-field vortex wake elements is to create a velocity field which alters the local angle of attack of the flow as percieved by the blade. More precisely, as far as the blade is concerned, this is equivalent to a change in the local pitch angle of the surface. This, of course, results in chordwise and spanwise variations of the local angle of attack since the vortex-induced velocity field varies from point to point along the blade. In equation (20), $\mathrm{d}\boldsymbol{l}$ is the length of the vortex segment, $\mathbf{r}$ is the position vector from the centre of the segment to an arbitrary point on the surface of the blade, and $\Gamma$ is the strength of the vortex segment. The velocity distribution calculated using equation (20) is singular at the centre of the vortex. To obtain physically realistic velocities whenever the blade is in close proximity to the BVI wake elements, a core region where the flow is rotational was modelled. In the present study, Scully's[5] core model was utilized to augment the vortex-induced velocities computed using equation (20).

*Trailing edge vortex sheet*

This sheet was assumed to coincide with the grid surface emanating from the blade's trailing edge and extending downstream to the outflow boundary. Note that there are two computational nodes (one on either side of the cut) for each physical plane point. Continuity of the physical flow properties across the wake cut was satisfied by averaging linear extrapolates of the computed flow field variables from above and from below the cut.

*Modeling of far-wake effects*

To complete the numerical boundary value problem for the physical flow we must also account for the blade tip vortices, the remainder of the wake system which lies outside the computational region, and any wake elements which might have passed out of, and returned into the computational region. In our Euler computations, the influence of the far-wake was modelled in the form of an azimuthal and spanwise variation of an induced flow (or equivalently an induced angle of attack) at the quarter-chord line of the blade.[31–41] Note that this approach is justified since the relative distance between the blade and the far-wake spirals is large. This approach, however, is not suitable for modelling the influence of the near wake BVI vortex wake elements. In this study, the quarter-chord angles of attack were provided through a separate computation using the free wake model in the comprehensive rotor trim code CAMRAD.[7] Once the inflow angles were calculated at the computational spanwise stations (through spanwise and azimuthal interpolations), they were then converted into equivalent surface transpiration velocities. These velocities, in turn, were implicitly represented in the velocity vector **V** which appears in equations (18) and (19).

The simplified 'quarter-chord angle of attack approach' described above for modelling the far-wake influence on the rotor flow field is not suitable for modelling the influence of the tip vortices which are in close proximity to the blade's surface (BVI wake elements). This is primarily due to the large chordwise and spanwise variations in the vortex-induced velocities which characterize the encounters between the blade and the tip vortices. In our present approach to simulate BVI, the vortex-induced velocities were computed using the law of Biot–Savart. As a result, caution was practiced in the computation of the far-wake inflow angles as they must only reflect the influence of all the far-wake elements, minus the influence of the trailing vortex sheet, minus the influence of the selected BVI wake elements (and, hence, the terminology 'partial inflow angles'), viz.

$$\left\{\begin{array}{c}\text{partial}\\ \text{inflow}\\ \text{angles}\end{array}\right\}=\left\{\begin{array}{c}\text{total wake}\\ \text{system}\\ \text{inflow angles}\end{array}\right\}-\left\{\begin{array}{c}\text{near-wake}\\ \text{inflow}\\ \text{angles}\end{array}\right\}-\left\{\begin{array}{c}\text{BVI}\\ \text{inflow}\\ \text{angles}\end{array}\right\}$$

(CAMRAD) (CAMRAD) (EULR.BVI) (EULR.BVI)

This, of course, was carried out to avoid accounting twice for the influence of the near-wake, and the selected BVI wake elements (once in CAMRAD and once in the Euler flow solver). In the next section, we describe in detail how the BVI wake elements are selected and then integrated into the time accurate Euler computations.

## VORTEX TRACKING

It is well-known that the influence of the rolled-up far-wake tip vortex on the local blade surface pressure variation is highly dependent upon:

1. the tip vortex strength

2. the vortex orientation with respect to the blade during blade passage
3. the minimum vortex-to-blade separation distance
4. the radial position and interaction azimuth
5. and the average blade loading.

These variables are defined for a given rotor by the flight condition and vehicle weight or thrust. As mentioned earlier, the lifting-line helicopter/rotor code CAMRAD was employed in the present work to compute the rotor trim state. More precisely, for the given rotor operating conditions, it was used to provide the free-wake geometry and tip vortex strength. The primary focus was placed on the BVI which occur in low-speed descent flight. Under these conditions, the tip path plane (TPP) angle and, in particular, the wake self-induced distortions play a significant role in affecting the axial position of the vortex wake elements. In the rotor plane, the vortex orientation is principally determined by the rotor advance ratio ($V_\infty/\omega R_{tip}$), with self-induced distortion having only a minor influence. The number of blades, of course, must also influence the number of possible blade/vortex encounters and their frequency.

Using CAMRAD, for the one-seventh scale AH1-OLS model rotor, we simulated the wind-tunnel descent flight conditions. A rigid blade dynamic model was employed with quasi-steady aerodynamics and free-wake inflow. The rotor was trimmed to meet a specified thrust, shaft angle, and zero flapping to duplicate the test conditions in the wind tunnel. To obtain adequate inflow at the moderately low advance ratios considered, three revolutions of vortex wake were modelled. In a prior study addressing the main rotor-tail rotor-wake interaction,[30] the CAMRAD code was modified to compute the wake geometry and inflow angles at 10° increments of rotor azimuth (rather than the standard 15° increment). In this study, the smaller azimuthal increments provided additional resolution of the BVI wake geometry and more accurate estimates of the vortex miss distances. The trim solution also allowed for three wake geometry iterations to ensure convergence of the final wake distortion.

In the course of this study, the CAMRAD predictions have indicated that numerous vortex interactions occur over many areas of the rotor disk. However, from an acoustics stand point, the most dominant interactions were those confined to the advancing side of the rotor disk where higher Mach numbers and dynamic pressures exist. The advancing blade will usually encounter tip vortex elements which have been deposited in the flow near the disk's leading edge by the preceding blade(s) or even by the same advancing blade during the preceding revolution. Those elements generated near the lateral edge of the rotor disk over the 90–130° azimuth range will be subject to upwash velocities resulting from the 'fixed-wing' nature of the wake roll-up which is typical of this region. Consequently, portions of these vortex lines will remain near, and perhaps be convected above, the rotor plane as they move downstream encountering the following blade tip. Consequently, the advancing blade tip may, therefore, encounter BVI conditions in level or even slightly ascending flight conditions. Once passed by a blade, the free tip vortex elements are then accelerated axially (in a direction normal to the tip path plane) due to the influence of the blade's bound vortex. This high rate of convection is generally maintained throughout the wake. As a result, the axial displacement of the wake tends to be larger after the first-blade passage.

A planform view of the CAMRAD-predicted OLS rotor wake at an advance ratio of 0·147 is illustrated in Figure 2. The figure depicts that the advancing blade will encounter five tip vortex lines during its sweep from the zero to the 180° azimuth positions. The axial position of each element in a trailed vortex line generally indicates its age since it was generated. For example, elements in the tip vortex designated III are closer to the rotor plane than those in the vortices labelled I and II. At approximately the 60° azimuth position, a near-parallel encounter occurs with the tip vortex designated I. This vortex line has been generated by the blade opposite to the

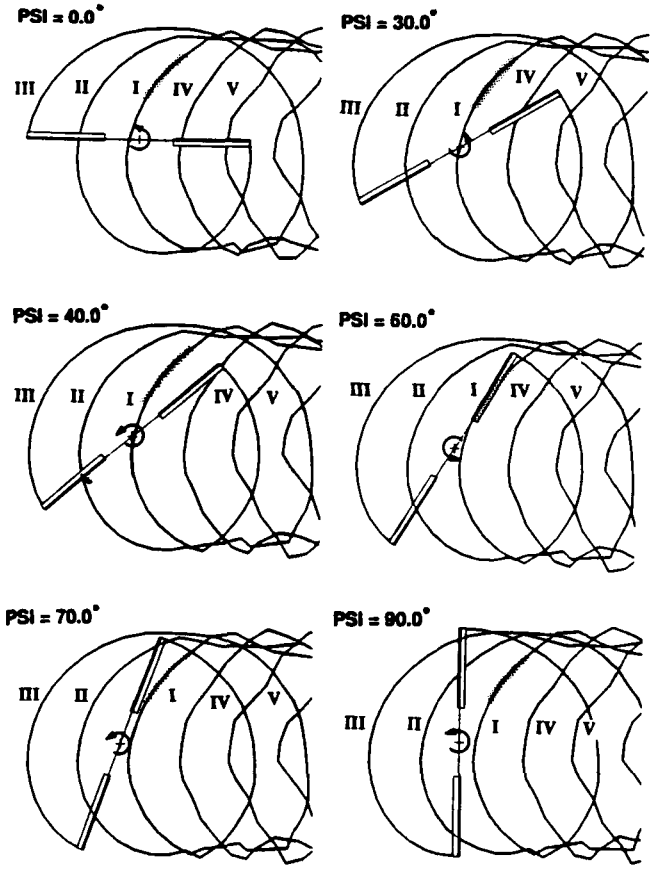


Figure 2. Planform view of the CAMRAD-computed tip vortex trajectories for the OLS model rotor (five blade–vortex interactions, $M_{tip}=0{\cdot}666$, $M_u=0{\cdot}147$, $r_v/c=0{\cdot}45$)

advancing blade (i.e. retreating blade) during its forward motion. Initially, it was thought that this interaction was a major contributor to BVI noise due to its parallelism. However, due to its age, high vehicle descent rates will be necessary before this vortex line approaches the rotor plane. The measured surface pressure data as well as our predictions tend to support this conclusion for all the descent rates considered.

Figures 3 and 4 illustrate the CAMRAD-predicted trajectories of the end points of a 'tracer' tip vortex element which have been deposited in the flow by the blade while at the 120 and 150° azimuth positions, respectively. Figures 3(a) and (3b) depict the time histories of the axial and radial convection distances of the tip vortex elements with respect to the rotor plane. In Figure 4, the rotor inplane convection distances are shown. The results shown in these figures reflect calculations made with both the free wake and the rigid wake model options available in CAMRAD. Our purpose here is to illustrate the influence of the wake self-induced and blade-induced distortions on the tip vortex trajectories. As seen, results from the use of the rigid wake model depict a constant convection rate in contrast to the more realistic variable convection rate which is predicted using the free wake model. The free wake trajectories in Figures 3(a) and 3(b)

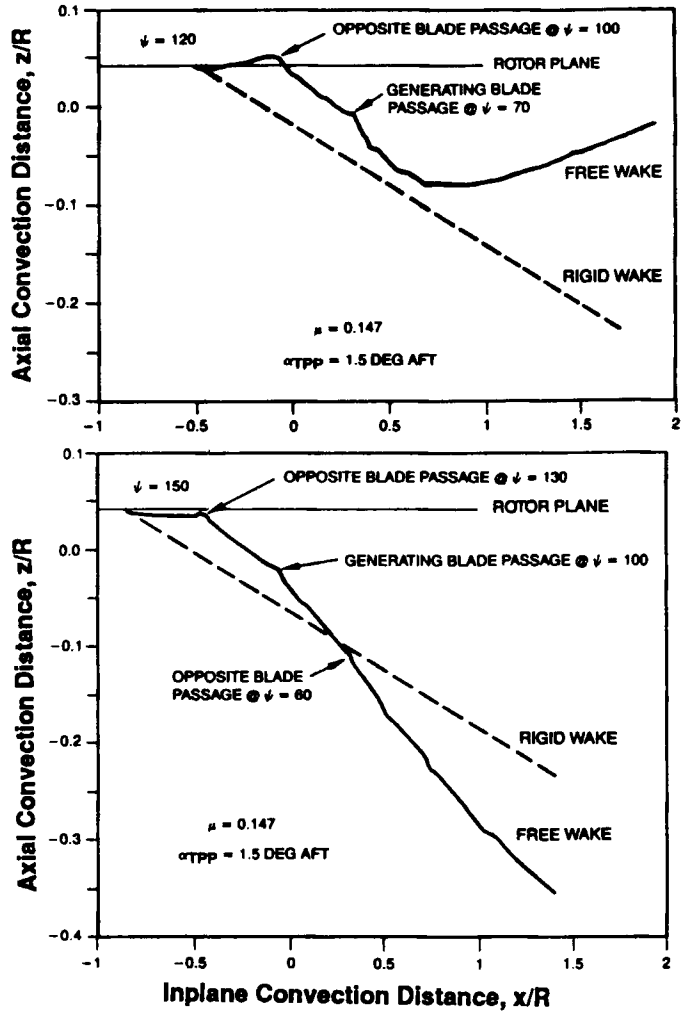


Figure 3. CAMRAD free and rigid wake model predictions for a 'tracer' tip vortex element (Rotor: OLS, $M_{tip}=0{\cdot}666$, $M_u=0{\cdot}147$, TPP = 1·5° aft)

also illustrate the changes in convection rates caused by repeated passage of the rotor blades as the tracer element 'drifts' aft from its original point of generation. Several blade passage points are indicated on the figures to illustrate the blade–vortex separation distances. In Figure 3(b), the wake element location denoted by 'opposite blade passage at 60°' corresponds to the parallel encounter of the blade with the tip vortex I shown in Figure 2. The large vortex–blade separation distance again confirms that the near-parallel blade–vortex encounter with vortex I will be weak in comparison to the other encounters with vortices II and III which are closer to the blades, see Figure 2.

Figures 5(a) and 5(b) illustrates the location of several BVI wake elements for the tip vortex lines I and II relative to the blade at the 50 and 70° azimuth positions, respectively. The upper portion of each plot depicts the planform geometry while the lower portion depicts an inplane view of the axial miss distance. The influence of the vortex core size on these distances is also shown. In

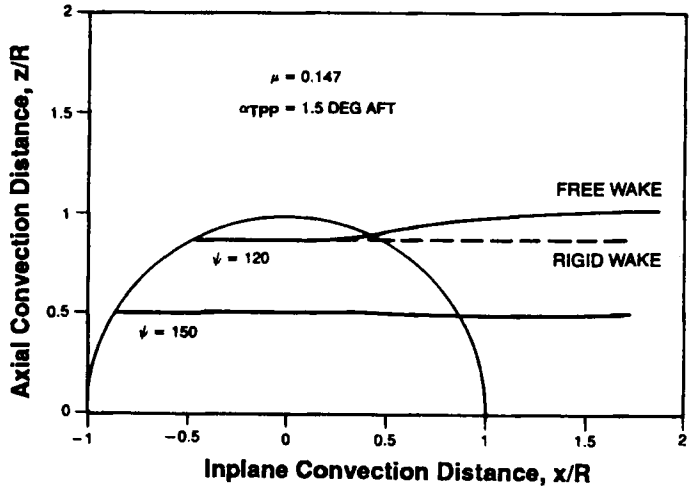


Figure 4. CAMRAD-predicted inplane convection of two 'tracer' tip vortex elements for the model OLS rotor ($M_{tip}=0{\cdot}666$, $M_u=0{\cdot}147$, TPP$=1{\cdot}5°$ aft)

previous correlation studies using CAMRAD,[11] we have found that a vortex core radius equal to 5% of the blade radius (or 45%$C$) provides the best correlation for the airloads. However, the use of this core size in the wake distortion calculations produces miss distances which result in head-on collisions with the blade. Numerical studies using the full potential formulation to model BVI have indicated that core radii of the order of 2% of the rotor radius (or 8% $C$) provide vortex miss distances which result in better correlations with the experimental data. For these reasons, the trim airloads were determined using a core radius of 45% $C$ while the wake geometry calculations were determined using a smaller core radius equal to 8% $C$. This option, available in the CAMRAD code, was exercised.

For given flight conditions, once a trimmed rotor state was obtained using the CAMRAD code, tracking of the BVI wake elements becomes a straight forward process. In this process, three inherent questions are answered. These relate to the vortex parameters, and the geometric orientation of the vortex with respect to the rotor blade. More precisely: How strong is the vortex element? How close does the element approach the surface of the advancing blade? How oblique is the vortex axis relative to the blade's leading edge? The answer to the first question relies entirely on the time-dependent load variation on the blade's surface, or alternatively on the spanwise circulation distribution. The question of blade–vortex separation distance, however, depends on two factors, namely, the user-specified vortex core size, and wake self-induced distortion. Since the tip vortex roll-up process was empirically modelled in CAMRAD rather than computed, the vortex core size became a user-specified parameter. The wake self-induced distortion was computed using the free-wake model within CAMRAD.

To answer the third of the above questions, planform plots of the tip vortex trajectories for different blade azimuthal positions was usually quite helpful in the identification of the specific interaction vortex elements. Figure 2 illustrates typical tip vortex trajectory planform plots at six positions of rotor azimuth. Clearly, one can identify an almost parallel interaction near the 57° rotor azimuth (vortex I), and an oblique interaction near the 70° azimuth position (vortex II). As seen, a third oblique interaction (with the vortex designated III) will occur as the blade continues to advance towards the 110° azimuth position. However, the vortices identified as vortices V and

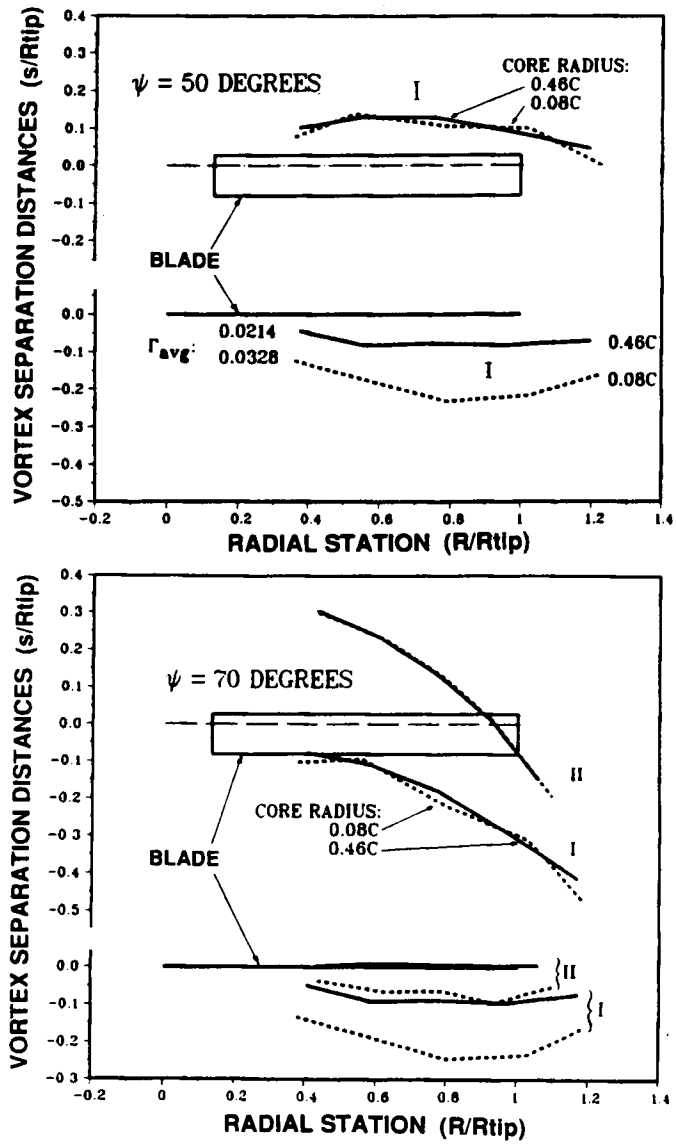


Figure 5. Planform and transverse views of the CAMRAD-computed BVI wake co-ordinates for the model OLS rotor ($M_{tip}=0{\cdot}666$, $M_u=0{\cdot}1477$)

IV result in a more or less perpendicular-type interaction (near the 0° azimuth) which predominantly affects the spanwise loading rather than the chordwise loading along the blade. In the present study, a tolerance relating to the degree of obliqueness of the vortex axis with respect to the blade's leading edge (not greater than 80.0°) was utilized to exclude modelling of the weaker perpendicular-type interactions.

Having identified the potential blade–vortex encounters, we next extract the trajectories of the selected vortex elements, as a function of rotor azimuth, from the geometric development of the

free wake. For instance, if two interactions were to be modelled, a minimum of five and a maximum of eight vortex segments were selected on each vortex element yielding either a total of ten or sixteen vortex segments to be modelled in the flow. Numerical experiments have indicated that the choice of five vortex segments was sufficient to preserve the curvature of the selected interaction vortex element. The extracted $x$, $y$ and $z$ coordinates of points representing the extremities of each vortex segment (referenced to the rotor shaft plane), and the strengths of the vortex segments were then cast in tabular format at 10° increments of rotor azimuth. This tabular data is later utilized by the Euler solver to model the details of the interactions.

## SOLUTION PROCEDURE

In this section, we outline how the CAMRAD-predicted far wake partial inflow angles, vortex wake strengths and trajectories are incorporated into the Euler calculations.

1. Using the far-wake partial inflow angles of attack, a quasi-steady solution is first computed at the 0° azimuth in preparation for the unsteady calculations.
2. In preparation for the unsteady calculations, interpolations are carried out among the CAMRAD-predicted vortex trajectories, and vortex strengths to determine the instantaneous positions and strengths of the various vortex segments with respect to the blade's surface which is assumed to lie in the rotor shaft plane.
3. The unsteady calculations are then started. Knowledge of the instantaneous relative position(s) of the identified BVI vortex element(s) with respect to the blade's surface allows the use of the Biot–Savart law to compute the vortex-induced velocities at all grid-point locations lying on the surface of the blade. This is repeated '$m \times n$' times for an '$m$' number of vortex interactions, and '$n$' vortex segments on each vortex element.
4. The sum of the normal components of the vortex-induced velocities are computed at the surface grid nodes and the surface slip (or condition of no flow penetration) boundary condition is modified in the Euler solver.
5. The unsteady Euler solutions are then found, respectively, using the hybrid ADI procedures discussed earlier.
6. The rotor is then advanced to the next azimuth position. If the final rotor azimuth position has not being reached (chosen to be 180°), steps 2–6 are repeated. Otherwise, the computations are terminated.

## RESULTS AND DISCUSSION

The results presented in this section were obtained using a grid having 121 nodes in the wrap-around direction (91 nodes on the aerofoil section), 24 radial stations with the outermost located at 20% radius beyond the rotor tip, and 21 grids in the normal direction. The body-conforming C-type mesh extended 3·5 chords ahead of the blade's leading edge, 6·3 chords beyond the blade's trailing edge, and had a maximum extent of 7·5 chords above the trailing edge 'wake cut' at the downstream outflow boundary. The solution procedure outlined above was applied in the simulations of supercritical BVI using an upstream-generated vortex,[1] and the self-generated subcritical BVI of References 22 and 23. Experimental data is also given to assess the relative accuracy of the predictions.

### *Parallel supercritical BVI model problem*

Figure 6 illustrates the experimental setup of Reference 1 where a non-lifting, rectangular, two-bladed rotor (0·5 ft chord, 3·5 ft radius) having a NACA0012 section interacts with an upstream-

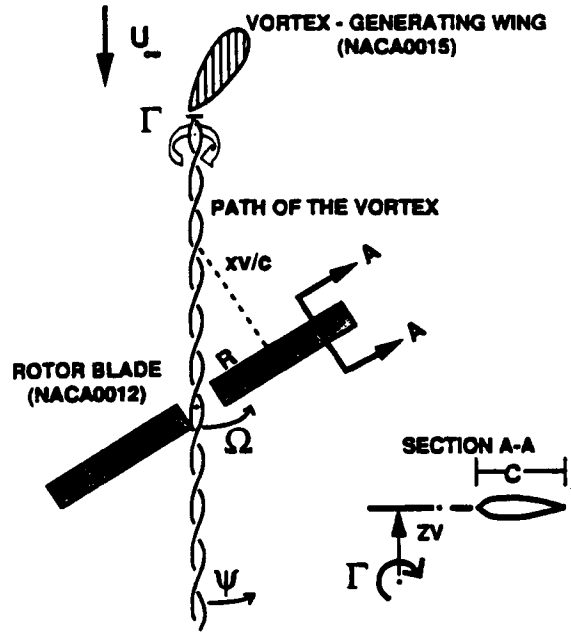


Figure 6. Experimental set-up for simulating parallel BVI using an upstream-generated vortex

generated vortex. At the 0°/180° azimuth positions the interaction is said to be a parallel one (the vortex axis is parallel to the blade's leading edge). In the experiments, a non-dimensional vortex strength $\Gamma$ (normalized using the product of the tunnel air speed and the chord of the vortex-generating wing) equal to $(0{\cdot}46 \pm 0{\cdot}20)$ was calculated using measured vortex-induced tangential velocities. The observed vortex core radius, $r_v$, was $0{\cdot}17C$ with $C$ being the blade chord length. In our simulations, we have assumed that the vortex is straight and that it has a finite length equal to four rotor radii.

Two geometric parameters will be used to indicate the relative position of the reference section along the rotor (located at the 89·3% span) with respect to the parallel interaction azimuth. The first parameter is the rotor azimuth angle '$\psi$' measured between the blade's leading edge and the zero-azimuth direction, see Figure 6. The second parameter, more appropriate for two-dimensional simulations, represents the upstream (or downstream) distance '$+x_v$' between the leading edge of the reference section and a line parallel to the vortex axis in the plane of the rotor blade. The $+/-$ signs associated with the distance $x_v$ are only intended to distinguish between instances where the vortex axes is located ahead $(-)$ or behind $(+)$ the leading edge of the reference section. The two parameters $\psi$ and $x_v$ are geometrically related via a simple relation viz.

$$x_v = R_{ref} \tan(180 - \psi).$$

The second parameter $x_v$ was utilized by Caradonna *et al.*[1] in their presentation of the experimental data. For consistency, it will also be used here.

Figure 7 depicts comparisons between the predicted and measured pressure distributions at the reference non-dimensional spanwise position for various rotor azimuth positions. In these simulations, the vortex miss distance $(r_v/C)$ was equal to $-0{\cdot}4$, the vortex strength was 0·30, the tip Mach number $(M_{tip})$ equal to 0·8, and the rotor advance ratio $(M_u)$ equal to 0·20. As seen, at the

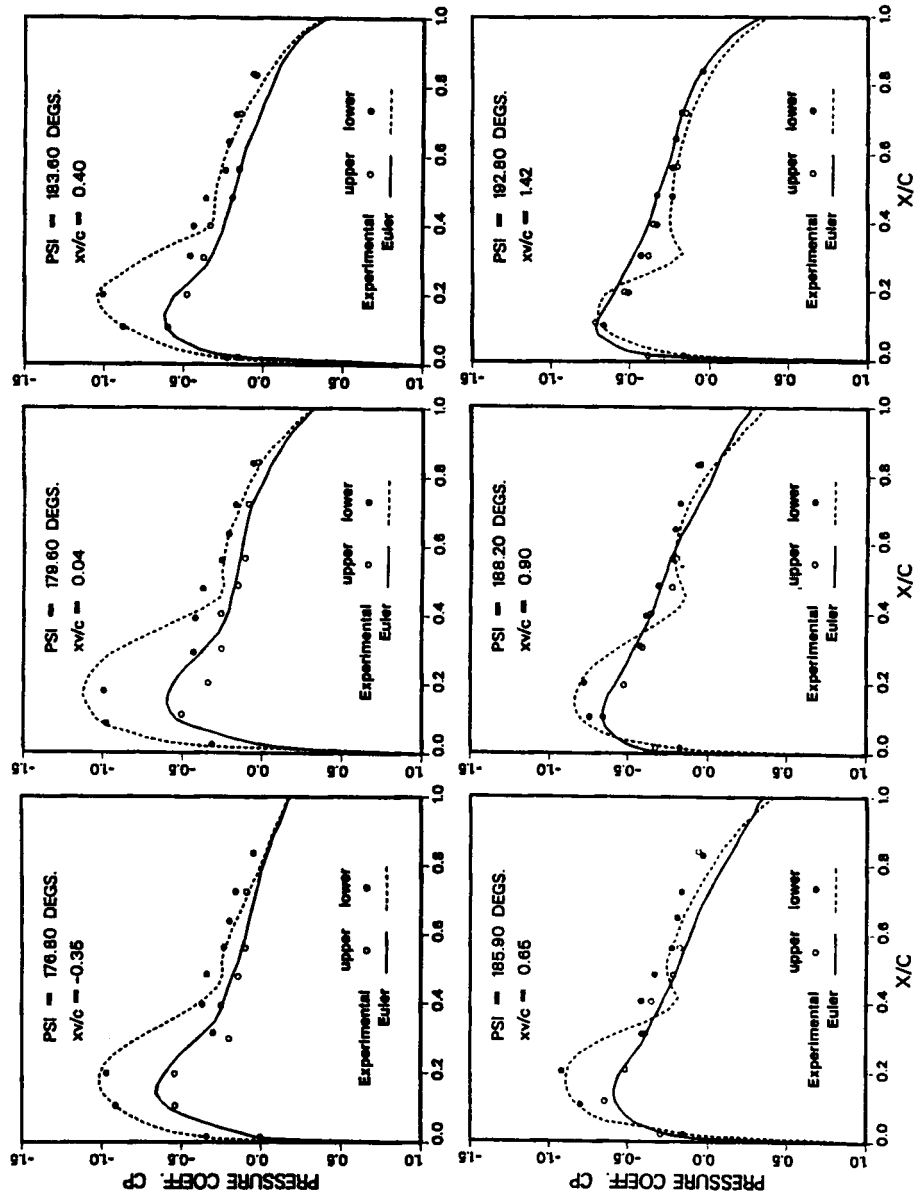


Figure 7. Predicted and measured pressure distributions for a non-lifting rectangular rotor blade during BVI using an upstream-generated vortex ($M_{tip}=0{\cdot}80$, $M_u=0{\cdot}20$, $R/R_{tip}=0{\cdot}893$, $r_v/C=0{\cdot}17$, $z_v/C=-0{\cdot}40$, $=0{\cdot}30$)

176·8° azimuth ($x_v/C = -0.346$), the vortex-induced velocities have resulted in a significant reduction of the pressure levels on the lower surface of the blade. The complete reversal of the upper- and lower-surface pressures is indicative of the negative sectional lift values attained at the reference radial station. Shock waves are also seen on the lower surface near the 25% chord station.

As the blade continues to approach the interaction azimuth, the reversal of the upper- and lower-surface pressures is further enhanced resulting in a minimum sectional lift value at the 179·6° azimuth (or equivalently $x_v/C = 0.04$). Recovery of the upper- and lower-surface pressures is also seen to occur as the blade's leading edge sweeps past the 180° interaction azimuth. Partial recovery is seen at the 185·9° ($x_v/C = 0.65$), and 188·2 ($x_v/C = 0.90$) azimuthal positions. As expected, this recovery process is initially felt near the blade's leading edge and progresses gradually towards the blade's trailing edge as the rotor continues to advance beyond the 180° azimuth. Note that the recovery in the sectional lift value for the reference section does not occur until the blade's trailing edge have completely passed the 0°/180° interaction azimuth. This observation is in agreement with the experimental observations of Reference 1. At this juncture, it is important to mention that in contrast to the supercritical BVI problem, studies of the subcritical parallel interaction problem[1,11] have indicated that lift recovery is usually achieved while the vortex is still in the vicinity of the blade's trailing edge (i.e. whenever $x_v/C$ is of the order of one). Of course, the exact position will depend on a number of factors among which we mention the vortex strength, vortex miss distance, and user-selected vortex core radius.

Referring to Figure 7 one notices that the overall features of the interaction have been captured using the Euler formulation. As seen, the lower surface shocks are well predicted (chordwise location). However, they are not as strong as one would infer from the experimental data. The expansion near the foot of the shock is also absent from the predicted surface pressures. Near the trailing edge, the predicted pressures are in agreement with the experimental data. Overall, the results seem to correlate well with the experimental data at these conditions. It should be noted that a 35% reduction in the measured vortex strength was necessary to obtain fairly good agreement between the predicted pressures and the experimental data. Similar reductions were also reported by Srinivasan, *et al.*[21] using the two-dimensional thin-layer Navier–Stokes equations, and by Strawn and Tung[42] using the three-dimensional full potential equation, in their studies of two- and three-dimensional parallel BVI, respectively. Numerical experiments using the Euler formulation have indicated a slight improvement in the predicted lower-surface pressures when using a vortex strength equal to 0·34 and a vortex core radius of 0·12.

Eighteen CPU minutes were required to perform this simulation on the CRAY X/MP computer.

### *Self-generated BVI*

*Case 1.* In this experiment, a lifting one-seventh scale AH1-OLS model rotor was allowed to interact with elements of its own generated wake. The experimental wind-tunnel conditions simulated low-speed descent flight at the rate of 300 ft/min with an advance ratio ($M_u$) of 0·13, a tip Mach number ($M_{tip}$) of 0·666, and a tip path plane (TPP) of 1° aft.

Figure 8 depicts comparisons between the predicted and measured differential pressures, in KPa, at a point located near the blade's leading edge ($x/C = 0.03$) for two user-specified vortex core radii ($r_v/C$) of 0·20 and 0·11. In these simulations, three blade–vortex encounters (resulting from the wake vortex elements I, II and III in Figure 2) were modelled in the Euler rotor flow solver. As seen, better correlation with the experimental data is obtained when using a vortex core radius of 0·11. In the present study, we have chosen to vary only the vortex core radius, among the other

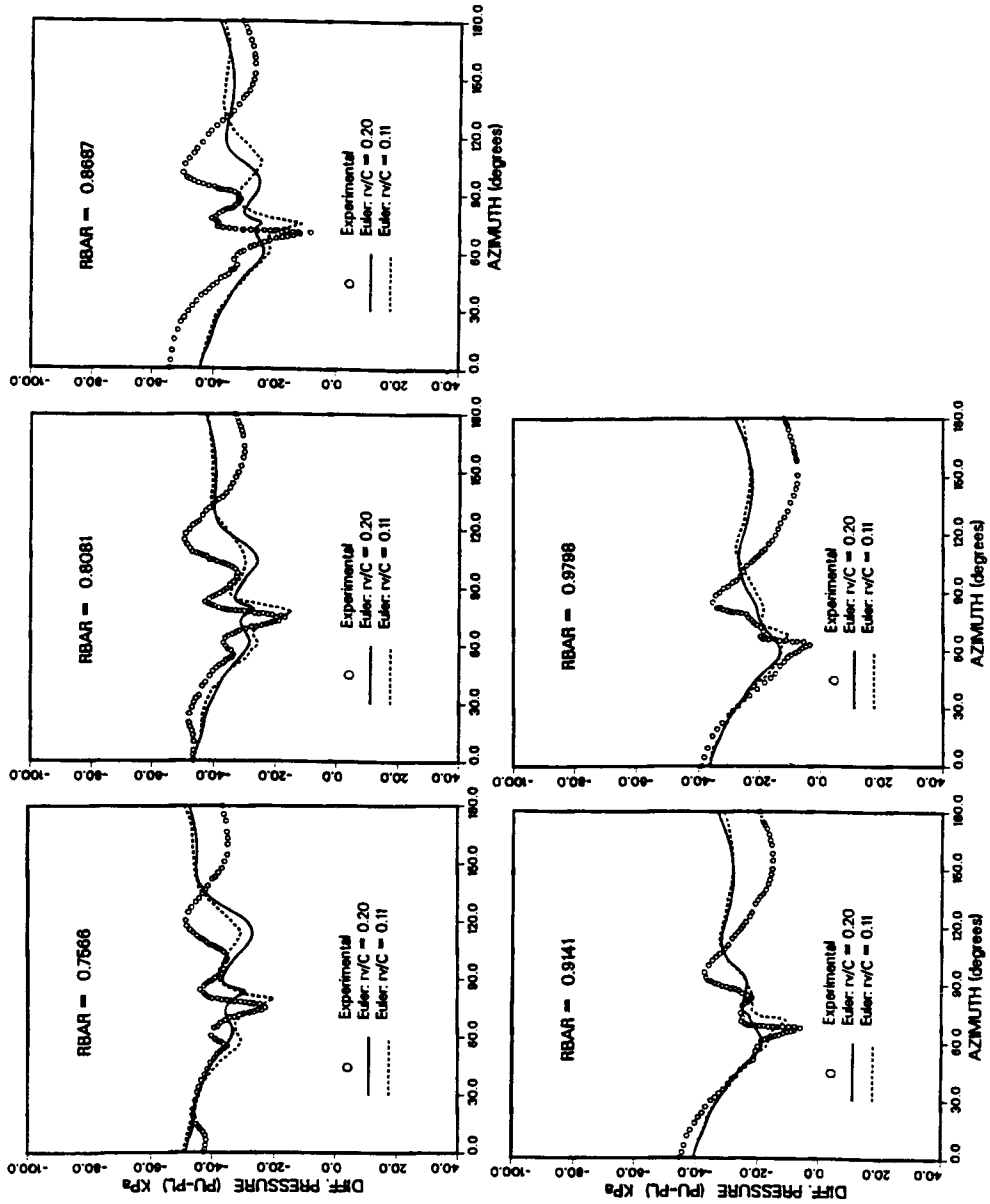


Figure 8. A comparison between the predicted and measured differential surface pressures for the model OLS rotor during self-generated BVI (3 vortex interactions, $M_{tip} = 0{\cdot}666$, $M_u = 0{\cdot}13$, TPP = 1° aft, $x/C = 0{\cdot}03$)

available vortex parameters, as means to improve the correlation with the experimental data. This is due to the fact that both the vortex strength, as well as the trajectories of the selected BVI wake elements, are dictated by the blade's load distribution (or thrust), and the rotor advance ratio.

One also notice that similar to the interactions resulting from an upstream-generated vortex, the self-generated interactions are also characterized by the rapid rise and drop of the leading edge pressures (or differential pressures) as the BVI wake elements pass by the blade's leading edge. This rapid variation of the leading edge differential pressures is also indicative of an associated rapid variation in the sectional lift and moment forces which are responsible for the increase in vibration and noise levels during blade–vortex encounters. Referring to Figure 8, one concludes that the second BVI, resulting from the encounter with the vortex designated II in Figure 2 is the most dominant among the three interactions being modelled. This, of course, is due to the very strong and rapid temporal variations of the measured and predicted leading edge differential pressures near the 78° azimuth. On the average, we have noticed that the CAMRAD-predicted time-dependent trajectory for the vortex designated II was closer (in vertical height) to the blade during its entire forward sweep (0–180°) as compared to the trajectories of the two vortices designated I and III in Figure 2. It should be mentioned here that the selected vortex core radius of 0·20 was based on the results of an earlier study by Hassan and Charles[11] which utilized the full potential formulation to model the self-generated BVI.

At the 91·4% and 97·9% radial stations, and for $r_v/C = 0{\cdot}20$, the predicted leading-edge pressures failed to capture the clearly visible strong interaction which occurs near the 66° azimuth position. Hassan and Charles, in an earlier study of BVI,[11] attributed the absence of these pressure peaks to the overprediction of the magnitude of the convective velocities (in a direction normal to the tip path plane) by CAMRAD. In Figure 8, for $r_v/C = 0{\cdot}11$, we illustrate the effects of artificially reducing (by 85%) the CAMRAD-predicted normal distances $z$ (which define the extremities of the last two segments on the selected BVI wake elements) on the accuracy of the predicted leading-edge differential pressures. Clearly, as a result of 'pushing' the BVI wake elements closer to the surface of the blade, a better correlation with the experimental data is obtained.

The discrepancies seen in Figure 8, and later in Figures 9 and 10, between the predictions and the experimental data beyond the 100° azimuth are partially attributed to the fact that the vortex core structure was kept invariant prior to and following the various encounters with the rotor blade. That is, as one would expect, a certain amount of distortion in the vortex core with the attendant diffusion of the vortex strength should take place as the blade encounters the vortex at a given azimuth. This is especially true if the average miss distance between the vortex and the blade is quite small (i.e., if $z_v$ is of the order of $0{\cdot}2C$). Fortunately, the most dominant BVI occurs near the 76° azimuth and as a result, the overall correlation up to this azimuth is fair. The first interaction at the 56° azimuth, though almost parallel, is relatively weak due to the large average vortex miss distance. However, as the rotor continues to advance beyond this azimuth, it encounters the second (most dominant), and then the third BVI wake elements (vortex elements II, and III of Figure 2). Realistically, following each one of these encounters, the structure of the vortices as well as their strength should have reflected a certain amount of distortion which is typically a function of the blade's advance ratio and average miss distance. In the present study, as well as in the studies of References 6, 8, 9, 11 and 18, the physics of these encounters were not modelled.

The simulations described above were performed on the CRAY X/MP computer. These simulations require, on the average, 22 CPU minutes for the unsteady calculations and 10 CPU minutes for the initial quasi-steady solution.

*Case 2.* In this simulation, two of the experimental conditions in case 1 were changed to reflect an increase in the rotor's advance ratio and tip path plane inclination to 0·147° and 1·5° aft,

respectively. For these conditions, Figure 9 depicts comparisons between the predicted and measured differential pressures for two vortex core radii when considering three BVI. Namely, those resulting from the vortices labeled I, II, and III in Figure 2. Slight variations in the CAMRAD-predicted vortex trajectories were noticed after comparisons were made with the trajectories predicted for case 1. These variations reflect the small differences in the experimental conditions for case 2 as compared to those of case 1. For $r_v/C = 0{\cdot}2$, the predicted pressures reveal a much weaker interaction than that depicted by the experimental data. However, for $r_v/C = 0{\cdot}11$, the overall features of the experimental data are captured except for the last two outboard stations where the predictions again fail to show any evidence of impulsive pressure variations. Similar to the results discussed in case 1, the discrepancies noticed in the tip region, especially at the 97·98% radial station, are attributed to the CAMRAD-predicted high velocities normal to the TPP which tend to convect the BVI wake elements further away from, rather than towards, the surface of the blade.

*Case 3.* The experimental conditions for this case are identical to those of cases 1, and 2 with the exceptions of: the advance ratio being equal to 0·1632, and the rotor tip path plane angle equal to 2° aft. Contrary to the previously discussed two cases, it is more evident here that the strongest BVI occur near the tip of the blade at the 98% radial station, see Figure 10. As seen, for $r_v/C = 0{\cdot}09$, the predicted pressures correlate quite well with the experimental data up to the 87% radial station and 90° azimuth. The correlation on the other hand is excellent near the blade tip at the 91% radial station up to the 70° azimuth, and at the 97·9% radial station up to the 45° azimuth.

In all the simulations conducted, we have noticed a consistent phase lag between the predicted and measured azimuthal positions of the BVI events. This phase lag, in turn, raises an important question which relates to the relative accuracy of the CAMRAD-predicted vortex trajectories. More precisely, our Euler results tend to support the fact that the CAMRAD-predicted streamwise convective velocities are somewhat smaller than what the experimental data implies. For example, in Figures 8–10 a shift of the order of 8–12° between the predicted and measured azimuth positions of the main BVI event near the 78° azimuth is clearly seen. This phase shift tends to be slightly smaller with the selection of small vortex core radii for the interaction wake elements. It is conjectured here that the lag of the predicted event behind the identical experimentally observed event is due to the underprediction of the streamwise convective velocities by CAMRAD. As a result, the CAMRAD-predicted vortex trajectories are slightly in error.

## CONCLUDING REMARKS

Based on the conservation form of the unsteady three-dimensional Euler equations, a numerical solution procedure was developed to analyse the model parallel BVI problem and the more realistic helicopter self-generated rotor BVI. The surface transpiration approach adopted in the present study to model vortex rotational effects have proven to be quite accurate and easy to implement in the Euler rotor flow slover. For supercritical interactions using an upstream-generated vortex, the results are in good agreement with the experimental data. For self-generated subcritical interactions, accuracy of the predicted leading edge pressures were found to rely heavily on the user-specified vortex core radius, and more importantly on the CAMRAD-predicted geometry of the interaction vortex elements and their relative orientation with respect to the blade. The results also suggest that the free-wake model used in CAMRAD, to predict the tip vortex trajectory for use in the Euler solution, yield lower streamwise, and higher axial (normal to TPP) wake convective velocities than those inferred from the experimental data.

The results presented have illustrated that certain discrepancies can only be overcome through improved modelling of the physical mechanism(s) involved in the distortion and the diffusion of

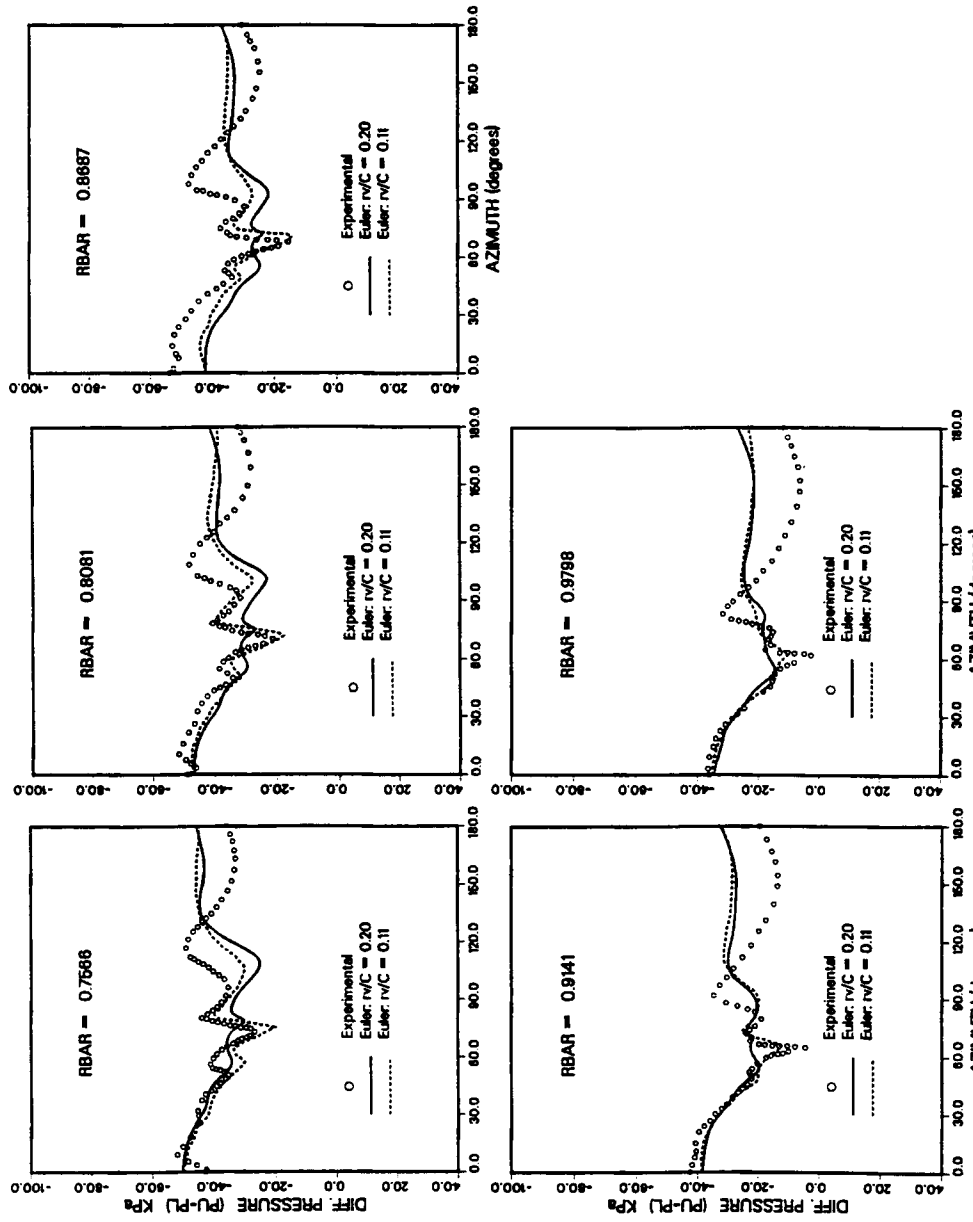


Figure 9. A comparison between the predicted and measured differential surface pressures for the model OLS rotor during self-generated BVI (3 vortex interactions, $M_{tip} = 0{\cdot}666$, $M_u = 0{\cdot}147$, TPP = 1·5° aft, $x/C = 0{\cdot}03$)

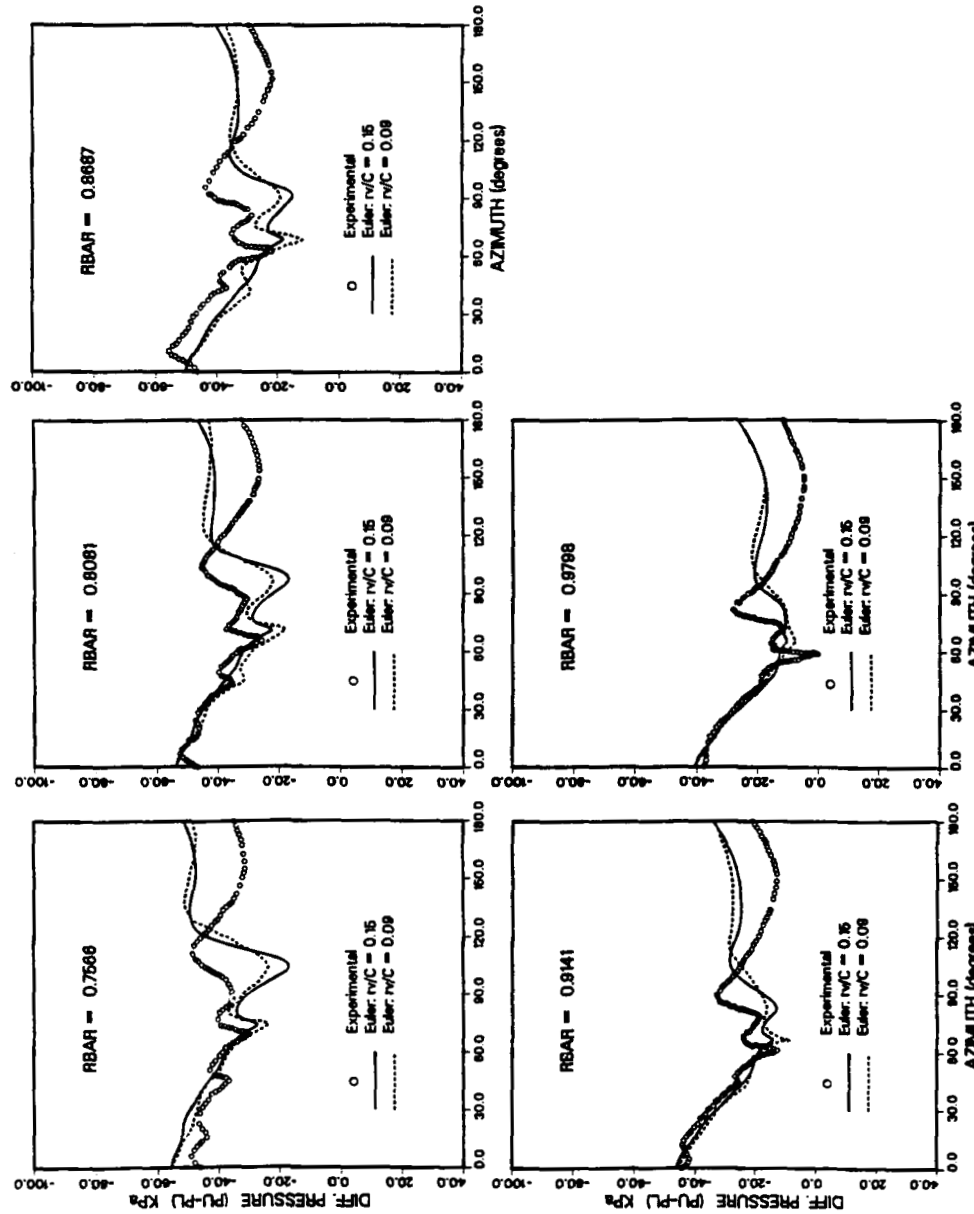


Figure 10. A comparison between the predicted and measured differential surface pressures for the model OLS rotor during self-generated BVI (3 vortex interactions, $M_{tip} = 0{\cdot}666$, $M_u = 0{\cdot}1632$, TPP = 2° aft, $x/C = 0{\cdot}03$)

the interaction vortex wake elements as they encounter the rotor blade. Fortunately, the accuracy of the most dominant interaction (peak amplitude, rate of variation of the leading-edge pressure) is unaffected by these factors as it takes place early in the first quadrant of the rotor disk. This is particularly important if the acoustic signature of the rotor is to be accurately predicted.

The computer resources required using the present approach are considered moderate and are by no means comparable to those required by the more efficient full potential BVI solvers. The results presented have proven the necessity of using an Euler-based formulation in the modelling of supercritical blade vortex interactions, especially if strong shock waves are to be accurately predicted.

## ACKNOWLEDGEMENTS

The authors would like to thank Bruce Charles of the McDonnell Douglas Helicopter Company for providing the vortex wake trajectories, and D. Boxwell, F. Caradonna of the Aeroflightdynamics Directorate at NASA Ames for providing the experimental data. This work was supported under the Independent Research and Development programme of the McDonnell Douglas Helicopter Company.

## REFERENCES

1. F. X. Caradonna, G. H. Laub and C. Tung, 'An experimental investigation of the parallel blade–vortex interaction', Presented at the 10th European Rotorcraft Forum, The Hague, Netherlands, 28–31, August 1984.
2. F. X. Caradonna, J. L. Lautenschlager and M. J. Silva, 'An experimental study of rotor–vortex interactions', *AIAA Paper 88–0045*, 1988.
3. A. Kokkalis and R. A. McD. Galbraith, 'Description of, and preliminary results from, a new blade–vortex interaction test facility', Presented at the 12th European Rotorcraft Forum, Garmisch-Partenkirchen, West Germany, September 1985.
4. A. Kokkalis and R. A. McD. Galbraith, 'Results from the Glasgow university blade–vortex interaction (B.V.I.) facility', Presented at the 13th European Rotorcraft Forum, Arles, France, September 1987.
5. M. P. Scully, 'A method of computing helicopter vortex wake distortion', Aeroelastic and Structures Research Laboratory, Massachusetts Institute of Technology, *Report ASRL TR-138-1*, June 1967.
6. G. R. Srinivasan, 'Computations of two-dimensional airfoil–vortex interactions', *NASA CR-3885*, May 1985.
7. W. Johnson, 'A comprehensive analytical model of rotorcraft aerodynamics and dynamics. Part 1: Analysis and development', *NASA TM-81182*, June 1980.
8. L. N. Sankar and J. B. Malone, 'Unsteady transonic full potential solutions for airfoils encountering vortices and gusts', *AIAA Paper 85–1710*, 1985.
9. H. E. Jones, 'The aerodynamic interaction between an airfoil and a vortex in transonic flow', Workshop on Blade–Vortex Interactions, NASA Ames Research Center, Moffett Field, California, October 1984.
10. L. N. Sankar and C. Tung, 'Euler calculations for rotor configurations in unsteady forward flight', Presented at the 42nd Annual Forum of the American Helicopter Society, June 1986.
11. A. A. Hassan and B. D. Charles, 'Simulation of realistic rotor blade–vortex interactions using a finite-difference technique', *AIAA Paper 89–1847*, June 1989.
12. A. A. Hassan and B. D. Charles, 'Numerical simulations of three-dimensional rotor blade–vortex interactions', *Proc. 3rd Int. Congress of Fluid Mechanics*, Cairo, Egypt, January 1990, Vol. II, pp. 745–749.
13. E. M. Murman and P. M. Stremel, 'A vortex wake capturing method for potential flow calculations', *AIAA Paper 82–0947*, 1982.
14. P. M. Stremel, 'A method for modeling finite core vortices in wake flow calculations', *AIAA Paper 84–0417*, 1984.
15. A. R. George and S. B. Chang, 'Flow field and acoustics of two-dimensional transonic blade–vortex interactions', *AIAA Paper 84–2309*, 1984.
16. A. R. George and A. S. Lyrintzis, 'Mid-field and far-field calculations of blade–vortex interactions', *AIAA Paper 86–1854*, 1986.
17. J. Steinhoff and K. Suryanarayanan, 'The treatment of vortex wakes in compressible potential flow', *Proc. AIAA Symp. on Computational Fluid Dynamics*, July 1983.
18. J. D. Baeder, W. J. McCroskey and G. R. Srinivasan, 'Acoustic propagation using computational fluid dynamics', *Proc. 42nd Annual Forum of the American Helicopter Society*, June 1986, Washington, D.C., pp. 551–562.
19. F. X. Caradonna, R. C. Strawn and J. O. Bridgeman, 'An experimental and computational study of rotor–vortex interactions', Proceedings of the 14th European Rotorcraft Forum, Milan, Italy, September 1988, pp. 18.1–18.16.

20. M. Damodaran and D. A. Caughey, 'Finite-volume calculation of inviscid transonic airfoil–vortex interaction', *AIAA J.*, **26**(11), 1346–1353 (1988).
21. G. R. Srinivasan, W. J. McCroskey and J. D. Baeder, 'Aerodynamics of two-dimensional blade–vortex interaction', *AIAA J.*, **24**(10), 1569–1576 (1986).
22. D. A. Boxwell, F. H. Schmitz, W. R. Splettstoesser and K. J. Schultz, 'Model helicopter rotor high-speed impulsive noise: measured acoustics and blade pressures', Presented at the 9th European Rotorcraft Forum, Stresa, Italy, September 1983.
23. F. H. Schmitz, D. A. Boxwell, W. R. Splettstoesser and K. J. Schultz, 'Model rotor high-speed impulsive noise: full-scale comparisons and parametric variations', *Vertica*, **8**(4), 395–422 (1984).
24. B. E. Wake and L. N. Sankar, 'Solutions of the Navier–Stokes equations for the flow about a rotor blade', Presented at the National Specialist Meeting on Aerodynamics and Aeroacoustics, Arlington, Texas, February 1987.
25. A. Jameson, 'Iterative solutions of transonic flow over airfoils and wings including flows at mach 1', *Comm. Pure Appl. Math.*, **27**, (1974).
26. R. M. Beam and R. F. Warming, 'An implicit factored scheme for the compressible Navier–Stokes equations', *AIAA J.*, **16**(4), 393–402 (1978).
27. T. H. Pulliam and J. L. Steger, 'Implicit finite-difference simulations of three-dimensional compressible flow', *AIAA J.*, **18**(2), 159–167 (1980).
28. T. H. Pulliam and J. L. Steger, 'Recent improvements in efficiency, accuracy, and convergence for implicit approximate factorization algorithms', *AIAA Paper 86–0360*, 1986.
29. Y. M. Rizk and D. S. Chausee, 'Three-dimensional viscous flow computations using a directionally hybrid implicit–explicit procedure', *AIAA Paper 83–1910*, 1983.
30. G. W. Hedstrom, 'Nonreflecting boundary conditions for nonlinear hyperbolic systems', *J. Comput. Phys.*, **30**, 222–237 (1979).
31. I. C. Chang, 'Transonic flow analysis for rotors. Part I: Three-dimensional unsteady full potential calculation', *NASA TP-2375*, 1984.
32. I. C. Chang, 'Transonic flow analysis for rotors. Part II: Three-dimensional quasi-steady full potential calculation', *NASA TP-2375*, 1985.
33. R. C. Strawn and F. X. Caradonna, 'Numerical modeling of rotor flows with a conservative form of the full potential equation', *AIAA Paper 86-0079*, 1986.
34. F. X. Caradonna and C. Tung, 'A review of current finite-difference rotor flow methods', Presented at the 42nd Annual Forum of the American Helicopter Society, June 1986.
35. F. X. Caradonna, A. Desopper and C. Tung, 'Finite-difference modeling of rotor flows including wake effects', Paper No. 2.7, Eighth European Rotorcraft Forum, Aix-en Provence, France, August 1982.
36. R. C. Strawn and J. O. Bridgeman, 'An improved three-dimensional aerodynamics model for helicopter airloads prediction', *AIAA Paper 91–0767*, 1991.
37. I. C. Chang, 'Unsteady Euler solution of transonic helicopter rotor flow', Presented at the AHS Aerodynamics and Aerocoustics Specialists' meeting, February 1987.
38. R. K. Agarwal and J. E. Deese, 'An Euler solver for calculating the flowfield of a helicopter rotor in hover and forward flight', *AIAA Paper 87–1427*, 1987.
39. I. C. Chang and C. Tang, 'Euler solution of transonic flow for a helicopter rotor', *AIAA Paper 87–0523*, 1987.
40. R. K. Agarwal and J. E. Deese, 'Navier–Stokes calculations of the flowfield of a helicopter rotor in hover', *AIAA Paper 88–0106*, 1988.
41. G. R. Srinivasan and W. J. McCroskey, 'Navier–Stokes calculations of hovering rotor flowfields', *J. Aircraft*, **25**, 865–874 (1988).
42. R. C. Strawn and C. Tung, 'The prediction of transonic loading on advancing helicopter rotors', Presented at the AGARD/FDP Symposium on Applications of Computational Fluid Dynamics in Aeronautics, Aix-en-Provence, France, April 1986.